e-ISSN: 2320-4230, p-ISSN: 2961-6085

Journal of Drug Discovery and Therapeutics

Available Online at www.jddt.in

CODEN: - JDDTBP (Source: - American Chemical Society)

Volume 11, Issue 4, July-August: 2023, 59-67

Research Article

Numerical Investigation of Some over an Inclined Plant

Ch. Shivaprasad[1], Dr. Deepika Vats[2]

[1]Research Scholar, Sunrise University, Alwar

[2]Professor, Sunrise University, Alwar

Article Info: Received: 20-05-2023 / Revised: 07-06-2023 / Accepted: 23-07-2023

Corresponding author: Ch. Shivaprasad

Conflict of interest: No conflict of interest.

Abstract:

The breakdown of geological material, particularly jointed rock masses, is a common source of difficulty for engineers. Triaxial compression experiments are performed on rock-like materials with parallel opening faults to examine the effect of confining load and inclination angle on cracking behavior and failure mechanism. Tensile failure and tensileshear failure are the two patterns, and they occur with equal regularity. There are nine fracture modes outlined, however the one most unique to samples with = 60° under high confining pressure is mode 8. Samples with = 60° have the lowest compressive strength and internal friction from the tests, whereas samples with = 65.31° have the lowest from the revised theory. When the inclination angle is between 0 and 60 degrees, the compressive strength drops; however, when the inclination angle is more than 60 degrees, the strength rises.Here, we report the results of an experimental and computational investigation into the comfort implications of turbulent jets from lobed diffusers. The primary objective is to maximize the effectiveness of air diffusion, the driving flow of ventilation in the occupancy zone, at the lowest possible cost. The tests have been carried out in a chamber with dimensions that allow for optimal performance under the challenging circumstances of a free and hot vertical jet being pushed against the wall. During the studies, the chamber has been sealed off from the outside world. Changes to the temperature of the blowing jet have reduced the temperature differential between the jet and its surroundings.

Key words: Lobed jet, thermal homogenization,comfort, experimental study, numerical simulation

Introduction

There is a close connection between the mixing processes and the onset of turbulence. Both the genesis and the transition of a flow are profoundly affected by its shape and the first disturbances. There is a plethora of uses for jet-based mixing. Plane reactor propulsion, pollution dispersion, HVAC systems, and other home heating and cooling systems are all examples. For maximum user comfort, it is also important that the air be pumped at a low rate into homes in a spatially uniform manner.

We suggest a "passive" method, consisting of blowing the jet via a lobed diffuser, to increase the effectiveness of air diffusion at

minimal cost, while also taking into mind the aesthetic element in the design of the air diffusion terminal units. This geometry has been used successfully in aerospace and aeronautics. Ejectors are components added to reactor outputs during the design process. When designing injectors that provide reliable combustion, they are also employed. This passive regulation makes it possible to enhance the building's air circulation.

No shortening of the jet range was necessary to achieve the reported induction increase. This is because the vein contracts near the blowing outlet, causing a surge in flow velocity. The flow seems to rotate as large secondary structures form in the lobed nozzle's trough. The induction efficiency of the lobed jet is improved because to the axes-crossing phenomena. To further enhance global performance, it is possible to tune the diffuser's elementary lobed orifice shape.

Literature Review

M. Imran(2019) In this research, we study the boundary layer flow of micropolar nanofluids across a linearly inclined stretched surface subjected to a magnetic field. This research makes use of Buongiorno's model for the thermal efficacy of the fluid flow when Brownian motion and thermophoresis features are present. In order to investigate the heat and mass exchange phenomena, the nonlinear problem for micropolar nanofluid flow across an inclined sheet is created, with special attention paid to the role that predictive flow parameters play in reinforcing the boundary layers. Through the use of appropriate similarity transformations, the governing nonlinear partial differential equations are transformed into nonlinear ordinary differential equations, which may then be solved numerically using the Keller-Box technique. The available findings are compared with the setup outcomes obtained without the included impacts, and a reasonable compromise is reached as a consequence. Tables and graphs display the numerical and graphical results as well.

L. Eljamali∗ and R. Sehaqui (2020) This research study analyzes the effects of a magnetic field applied perpendicular to the cavity's plane on the natural convection of a water-copper nanofluid within an angled enclosure. Assumably, the cavity's vertical side walls are heated at a different rate than the horizontal ones. Stream function and vorticity are introduced as new variables in the reformulated governing equations. An alternating direction implicit (ADI) approach is then used to numerically solve the resultant boundary value issue. The streamlines and isotherms, as well as the impact of the Hartmann number and the Rayleigh number, are shown in a number of different charts.

Uddhaba Biswal(2022) In this piece, we'll look at what happens to a nanofluidic water solution as it flows between two inclining planes that are allowed to expand and contract. To manage governing coupled nonlinear DEs, the Optimal Homotopy Analysis Method (OHAM) has been used here. The convergence controller settings in OHAM have been calculated using a method that reduces computational complexity while maintaining accuracy. The numerical results obtained for varying the number of terms in the series solution are used to visually demonstrate the convergence of the proposed technique. The accuracy of the current findings has been checked by comparing them to the numerical outcomes of the standard MATLAB solver, BPV4C. The Nusselt number and the coefficient of skin friction calculated with the current technique have also been compared to those calculated using the traditional approach. Furthermore, by computing residual errors for consecutive approximations, the correctness of the resulting findings has

been demonstrated. Calculations demonstrate convergence of the resulting findings to within three decimal places, with residual errors approaching zero throughout four approximation terms. Finally, a graphic is shown showing the impact of altering a single physical parameter with all other factors held constant on the resulting velocity and temperature profiles. All permutations, including but not limited to, decreasing walls with converging channels, extending walls with diverging channels, and so on, are taken into account. The essay focuses mostly on the effects of the stretch and shrink parameters. In both the divergent and convergent examples, the findings demonstrate that raising the stretching/shrinking parameter raises the velocity value and reduces the temperature value.

Julian Brosda(2021) This research focuses on the secondary currents created by turbulent flow in a partially filled conduit. As far as the authors are aware, this is the first highly resolved data-set for semifilled-pipe flow generated by direct numerical simulation. The turbulence levels may be kept at a minimum with a value of Re=115, and they can be kept at a moderate level with a value of Re=460. Some of the most prominent features of the flow, including the velocity-dip phenomena, the primary secondary flow, and the qualitative distribution of the Reynolds stresses in the core, are consistent with previously reported findings from experiments. Some of the flow phenomena we see have not been previously documented in the literature. The distribution of wall shear stress throughout the perimeter is influenced in large part by the inner secondary cell at the mixed corner between the free surface and the wall of the pipe. We find that the location and size of the inner vortex are proportional to the wall shear stress, whereas the outer vortex's properties are proportional to the external factors. Distributions of the whole Reynolds stress tensor and its anisotropy, which causes the creation of mean streamwise vorticity in a constrained area near the pipe's mixed corners, are shown and discussed for the first time. The stagnation point between the inner and outer vortices is where the secondary kinetic energy is created on average at the free surface. A vortex dynamics process suggested in the literature is consistent with this generating mechanism.

Chandra Pal, Gopal (2018 Using a two-dimensional porous enclosure with two heated circular cylinders inserted at various places along the vertical mid-plane, the current work quantitatively analyzes the features of erratic heat transport and entropy formation. Lower Darcy numbers (104) see heat transmission largely as conduction, whereas higher Darcy numbers (103, 102) see heat transfer through convection becoming prominent. Time-average Nusselt number shows contrasting behavior with respect to interspacing distance. At small values of the Darcy number, irreversibility is primarily caused by the creation of entropy as a result of heat transfer; at greater Darcy numbers, irreversibility is influenced by the Rayleigh number.

Methods

Specimen’s preparation

Cement mortar has been shown to be an appropriate rock-like material for rock mechanics tests due to its ability to mimic the brittle failure properties of rock mass with non-consecutive joints. Triaxial loading tests were performed on specimens produced from C32.5 Portland cement, fine sand, and water for this investigation. Table 1 displays the mechanical characteristics of the rock-like substance that was created by combining cement, sand, and water in a weight ratio of 1:2:0.4. Fine sand with a particle size of less than 1 mm was used to

lessen the impacts of heterogeneity brought on by the creation of weak structural surfaces during the preparation process.

Mechanical characteristics of the experimental material are listed in Table 1.

Type	UCS	Young's modulus	Poisson's ratio	Cohesion	Friction angle
	σ_c (MPa)	E (GPa)	v	c (MPa)	φ (°)
Sandstone	20–170	3–35	0.02–0.20	4–40	25–60
Rock-like material	21.88	6.45	0.15	4.37	37.95

Compressive strength in just one direction; UCS**.**

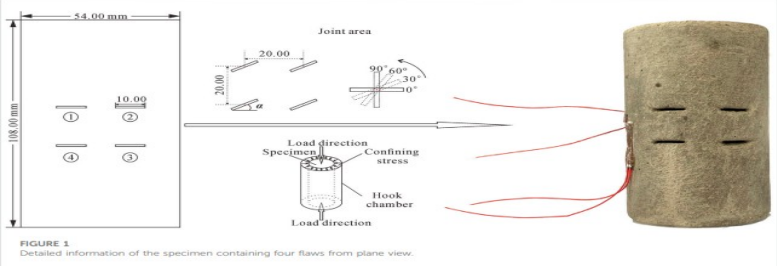

Figure 1: Detailed information of the specimen containing four flaw from plane view.

Flat sheet of steel (10 mm in width, 1 mm in thickness) was prefabricated, then fastened in place, just as planned. To prevent the samples from shrinking unevenly due to dehydration and cement hydration, they were cured for 28 days in a tank at 20°C. Each specimen has two strain gauges connected to it, one measuring vertical strain and the other measuring horizontal strain. Figure 1 depicts the specimen geometry as a cylinder, with a height of 108 mm and a radius of 54 mm. The distance in millimeters between any two neighboring centers of the four preexisting defects is constant at 20 mm. Figure 1 depicts the inclination angle. In this study, we calibrate microscopic parameters in numerical simulation by comparing the behavior of five types of jointed specimens, each of which is made up of faults with varied inclination degrees. These samples make it easy to see how defects transform into transfixion in response to loads.

Testing procedure

The ELE apparatus was used to perform triaxial compression tests with a loading rate of 0.1 0.2 kN/s till specimen failure. Force equality was ensured by aligning the centers of the Hooke chamber and the jack before loading. The confining stress was varied from 2.0 to 10.0 MPa throughout five different levels of experimentation. Prefabricated defects at 0 degrees, 30 degrees, 60 degrees, and 90 degrees were used to study the effect of this parameter**.**

Results and Discussion

The flow properties and heat transmission of MHD nanofluids are primarily influenced by the magnetic field strength, the enclosure's inclination angle, and the nanoparticle volume fractions. Nusselt number, temperature profile, velocity profile, and isotherm distributions are all shown here in an effort to analyze the effects of these variables. The impact of the Rayleigh number on the flow structure is seen in Figure 2. Take note of the clockwise revolving, single-cell structure of the ascending streamlines.

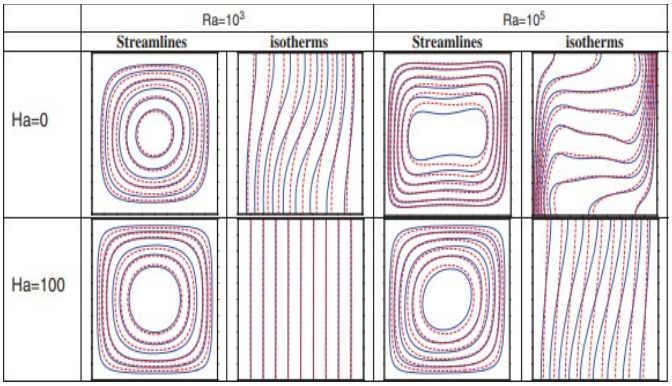

Figure 2: Streamlines and isotherms at different values of Rayleigh and Hartmann numbers

And descending down the frigid wall. In addition, when Ra = 103, the streamlines are roughly circular even when there is no magnetic field present (Ha = 0). At Ra = 105 (Ha = 0), a substantial shear is seen in the internal streamlines, and the concentricity begins to break down. There is a vertical symmetry in the flow from X = 0 5 to Ra = 103 when the magnetic field is present (Ha = 100). This symmetry breaks out at significant levels of the Rayleigh number (Ra = 105). We also find that for Ha = 0, the streamlines for the basic fluid (water) and the nanofluid (= 0 1) instances are essentially indistinguishable. However, the presence of nanoparticles (= 0 1) has a significant influence on the structure of the flow in the presence of the magnetic field (Ha = 100), especially at Ra = 105. Figure 4 depicts isotherms that represent the temperature field's distribution. As the Rayleigh number, Ra, increases, the convection currents get stronger, and the isotherms become distorted, especially at Ra = 105. In a magnetic field (Ha = 100), these latter tend to become parallel to one other, resulting in a heat transfer due to conduction. Not only that, but the effects of the nanoparticle addition are only noticeable for Ha = 0; Ra = 103 and Ha = 100; Ra = 106.

Figure 5 displays, given a selection of Ra and Ha values, the resulting temperature profiles along the central portion of the hot wall. When Ra = 104, the temperature changes relatively linearly with x, but it changes very little with the magnetic field with higher Hartmann numbers. If the magnetic field is weak, the temperature profiles will display a counterclockwise and clockwise swing around this linear profile. We display the y component of velocity v profiles to evaluate the impact of both buoyancy and magnetic forces on velocity. For Ra = 104 (Fig. 6) and Ra = 106 (Fig. 4), the curves are shown in the middle of the hot wall. When the force field is accelerated, the result is a reduction in the speed's amplitude. An considerable velocity shift occurs in the vicinity of the adiabatic walls due to an increase in buoyancy force from Ra = 104 to Ra = 106. However, the fluid practically stops moving inside the core area with the higher Rayleigh number. In Figure 8, we see how the vertical component of the velocity changes as the angle of the cavity's inclination changes relative to the horizontal. All the lines intersect in the middle of the hollow at X = 05, which is the location where the speed of light is zero. It is important to notice, too, that in the neighborhood of the left wall, the highest

and lowest values of the velocity are achieved for.

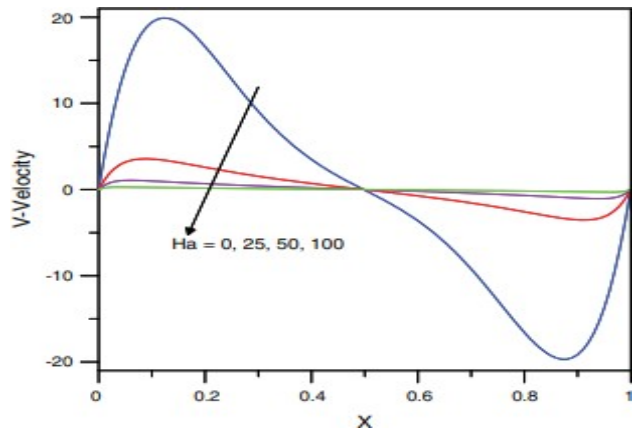

Figure 3: Velocity profiles along the middle of hot wall for Ra = 10

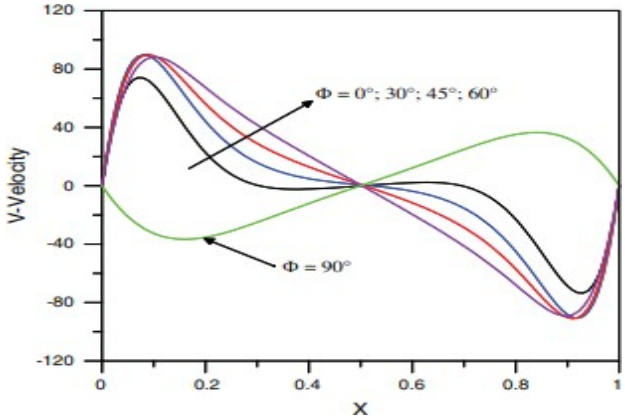

Figure 4: Velocity profiles along the middle of hot wall for different inclinations angle for = 0; Ha = 0 and Ra = 10

Each corresponding to an angle of 30 degrees and 90 degrees. The average Nusselt number varies with the inclination angle for various Hartmann values, as seen in Figure 9. The average Nusselt number tends to go down, as we can observe. The average Nusselt number also varies significantly with the angle of inclination for low Hartmann numbers, but less so for high Hartmann numbers.42-43 In Figure 10, we see how the presence or absence of a magnetic field affects the flow structure depending on the cavity's inclination angle. Take note of the single-cell morphology of the streamlines, which tends toward centrifugal uniformity as the angle of inclination of the cavity rises (with the exception of angle.

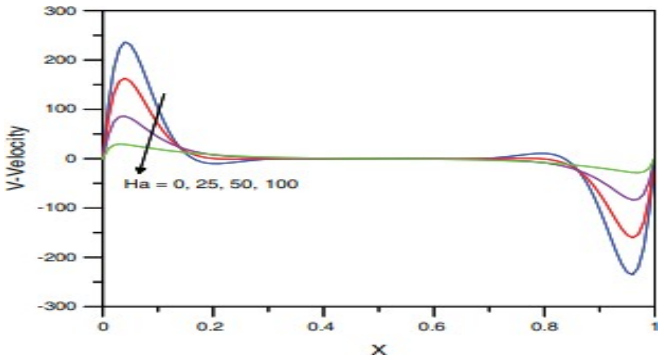

Figure 5: Velocity profiles along the middle of hot wall for Ra = 10.

In the absence of a magnetic field, a vertical temperature gradient in the cavity at an angle of 90 creates a flow within the enclosure of the Rayleigh-Bénard type. Ha = 100 maintains near-perfect symmetry with respect to the cavity's median plane at X = 0 5 through a central narrowing of the streamlines that becomes more significant as X = 30. This narrowing is most pronounced for the slowest-rotating, most interior streamlines. In the absence of the magnetic field (Ha = 0), we observe that the isotherms are significantly deformed by an increase in the inclination angle, with more and more hot fluid being displaced near the cold wall (and vice versa for the cold fluid) and thermal conduction being favored along the entirety of the active walls. In fact, the layered and dense isotherms rearrange themselves near the active walls, especially for = 30. When a magnetic field (Ha = 100) is present, the isotherm distribution does not change much depending on the cavity's orientation, and conduction-mode heat transfer is the norm.

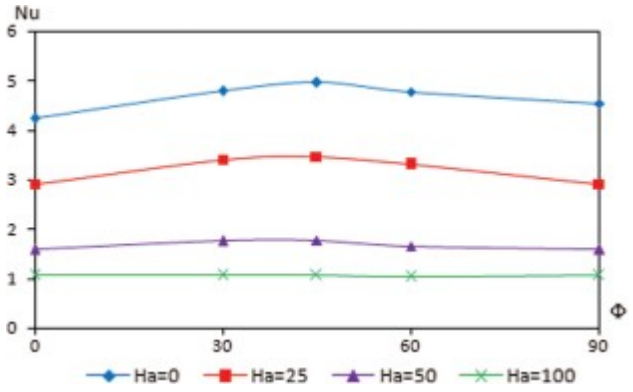

Figure 6: Effect of Inclination angle and Hartmann number on the average Nusselt number Ra = 105 ; = 0.

Conclusion

After subjecting rock-like specimens with four parallel defects to a triaxial compressive test, researchers discovered nine fracture modes and two failure patterns. Compressive strength and mechanical characteristics were summarized in relation to the angle of inclination. The accuracy of the revised theory of open-flawed rock mass fracture was tested by numerical biaxial experiments. There is no failure pattern

constituted of pure shear fractures, and the majority of cracks that start under triaxial strain are tensile. The tensile failure mode occurs twice as often as the tensile-shear failure mode. A 90-degree inclination angle indicates a tensile failure pattern in all of the samples. Shear fractures form progressively for materials with = 0°, 30°, and 60°, leading to tensileshear failure at high confining stress.

References

1. Rafique, Khuram & Imran, M. & Misiran, Masnita. (2019). Numerical Study on Micropolar Nanofluid Flow over an Inclined Surface by Means of Keller-Box. Asian Journal of Probability and Statistics. 1-21. 10.9734/ajpas/2019/v4i430122.
2. Biswal, Uddhaba & Chakraverty, S. & Ojha, Bata & Hussein, Ahmed. (2022). Numerical investigation on nanofluid flow between two inclined stretchable walls by Optimal Homotopy Analysis Method. Journal of Computational Science. 63. 101759. 10.1016/j.jocs.2022.101759.
3. Gopal Chandra Pal, Navneet Goswami & Sukumar Pati (2018) Numerical investigation of unsteady natural convection heat transfer and entropy generation from a pair of cylinders in a porous enclosure, Numerical Heat Transfer, Part A: Applications, 74:6, 1323-1341, DOI: 10.1080/10407782.2018.1507887
4. Zhou, Q. L. (1987). Compress shear fracture criterion of rock and its application.
5. Chin. J. Geotechnical Eng. 9, 33–37. (in Chinese).
6. Yao, W., Cai, Y. Y., Yu, J., Zhuo, J. F., Liu, S. Y., and Tu, B. X. (2019). Experimental and numerical study on mechanical and cracking behaviors of flawed granite under triaxial compression. Measurement 145, 573–582. doi:10.1016/j.measurement.2019.03.035
7. Wang, Y. X., Zhang, H., Lin, H., Zhao, Y. L., and Liu, Y. (2020). Fracture behaviour of central-flawed rock plate under uniaxial compression. Theor. Appl. Fract. Mech. 106, 102503–102518. doi:10.1016/j.tafmec.2020.102503
8. Wong, L. N. Y., and Einstein, H. H. (2009). Systematic evaluation of cracking behavior in specimens containing single flaws under uniaxial compression. Int. J. Rock Mech. Min. Sci. 46, 239–249. doi:10.1016/j.ijrmms.2008.03.006
9. Guo, S. F., Qi, S. W., Zou, Y., and Zheng, B. (2017). Numerical studies on the failure process of heterogeneous brittle rocks or rock-like materials under uniaxial compression. Materials 10, 378–390. doi:10.3390/ma10040378
10. Fu, J. W., Chen, K., Zhu, W. S., Zhang, X. Z., and Li, X. J. (2016). Progressive failure of new modelling material with a single internal crack under biaxial compression and the 3-D numerical simulation. Eng. Fract. Mech. 165, 140–152. doi:10.1016/j.engfracmech.2016.08.002
11. Cui, J., Jiang, Q., Li, S., Feng, X., Zhang, Y. L., and Shi, Y. E. (2020). Numerical study of anisotropic weakening mechanism and degree of non-persistent open joint set on rock strength with p
12. Cheng, Y., Jiao, Y. Y., and Tan, F. (2019). Numerical and experimental study on the cracking behavior of marble with en-echelon flaws. Rock Mech. Rock Eng. 52, 4319–4338. doi:10.1007/s00603-019-01849-x

13. Huang, Y. H., Yang, S. Q., and Zeng, W. (2016). Experimental and numerical study on loading rate effects of rock-like material specimens containing two unparallel fissures. J. Central South Univ. 23, 1474–1485. doi:10.1007/s11771- 016-3200-3

14. Le, H. L., Sun, S. R., and Wei, J. H. (2019a). Influence of types of grouting materials on compressive strength and crack behavior of rocklike specimens with single grout-infilled flaw under axial loads. J. Mat. Civ. Eng. 31, 1–6. doi:10.1061/ (ASCE)MT.1943-5533.0002554

15. Bobet, A., and Einstein, H. H. (1998). Fracture coalescence in rock-type materials under uniaxial and biaxial compression. Int. J. Rock Mech. Min. Sci. 35, 863–888. doi:10.1016/S0148-9062(98)00005-9.